Two-dimensional Rutherford-like scattering in ballistic nanodevices

S. Toussaint,[1,*] B. Brun,[1] S. Faniel,[1] L. Desplanque,[2] X. Wallart,[2] V. Bayot,[1] and B. Hackens[1,†]
[1]*Institute of Condensed Matter and Nanosciences (IMCN/NAPS), Université catholique de Louvain, B-1348 Louvain-la-Neuve, Belgium*
[2]*Université Lille, CNRS, Centrale Lille, ISEN, Université Valenciennes, UMR 8520-IEMN, F-59000 Lille, France*

(Received 26 March 2018; revised manuscript received 11 July 2018; published 24 August 2018)

Ballistic injection in a nanodevice is a complex process where electrons can be either transmitted or reflected, thereby introducing deviations from the otherwise quantized conductance. In this context, quantum rings (QRs) appear as model geometries: in a semiclassical view, most electrons bounce against the central QR antidot, which strongly reduces injection efficiency. Thanks to an analogy with Rutherford scattering, we show that a local partial depletion of the QR close to the edge of the antidot can counterintuitively ease ballistic electron injection. In contrast, local charge accumulation can focus the semiclassical trajectories on the hard-wall potential and strongly enhance reflection back to the lead. Scanning gate experiments on a ballistic QR and simulations of the conductance of the same device are consistent and agree that the effect is directly proportional to the ratio between the strength of the perturbation and the Fermi energy. Our observation fits the simple Rutherford formalism in two dimensions in the classical limit.

DOI: 10.1103/PhysRevB.98.075310

I. INTRODUCTION

Controlling collisions and scattering has always played an essential role in physics. Thanks to model experiments ranging from collisions of α particles with gold foil, conducted more than a century ago [1,2], to high-energy collisions between hadrons at the Large Hadron Collider [3], a wealth of detailed information was revealed about the nature of atoms and elementary particles as well as their interactions. In this framework, the most fundamental description of the interaction of a beam of particles and a scatterer is the famous Rutherford formula, describing the differential-cross-section dependence on the scattering angle, energy of the incident beam, and potential shape of the scatterer [4]. Collisions are also ubiquitous in solid-state physics, in particular when considering charge transport. Charge carriers indeed scatter on a large variety of "defects": lattice vacancies, phonons, the potential of remote ionized impurities, etc. Due to this complexity, it is almost impossible to reach the same degree of control in charge transport scattering experiments as in the case of collisions involving beams of elementary charged particles propagating in vacuum.

However, in the ballistic regime of charge transport, the bulk carrier mean free path becomes larger than the device size, and transport properties can be tailored by tuning the device geometry [5,6]. This is, of course, achieved most favorably in nanodevices, which are probably the most adequate system to attempt to perform "ideal" scattering experiments with electrons in solids and their associated quasiparticles. Nevertheless, even in the ballistic regime, full treatment of scattering in solid-state devices requires taking into account complex many-body interactions with the Fermi sea [7,8].

The archetypal ballistic device is the so-called quantum point contact (QPC). Thanks to a metallic split gate deposited on top of a semiconductor heterostructure hosting a high-mobility two-dimensional electron gas (2DEG), one can create a constriction whose width can be varied at will with gate voltage. The smooth resulting potential ensures adiabaticity, which leads to a quantized conductance of the QPC [9,10]. This canonical realization of ballistic transport allowed us to go one step further, in particular when combining transport measurements with a local electrostatic perturbation induced by a scanning probe. This method led us to explore deviations from this perfect picture of QPCs, such as the observation of branched electron flow in the leads and rich many-body physics [11–15]. In other studies, geometric scatterers with an asymmetric shape were designed to act as mirrors redirecting electrons towards a particular lead through specular reflection [16], leading to a rectifying behavior similar to diode bridges. Such devices could yield applications at high frequency, given the short electron transit time in the ballistic regime [17,18]. In addition, the magnetic field is a particularly useful knob to focus electrons at desired locations through the so-called magnetic-focusing effect [19,20]. In a surprising way, to our knowledge, there are many fewer examples where fine tuning of the electrostatic potential is used for similar lensing purposes [21].

Here, we study the geometry presented in Fig. 1 where specular electron reflection on the hard wall facing the entrance of a quantum ring (QR) is either enhanced or reduced by tailoring the local electrostatic potential in the vicinity of the wall. The idea is that a Rutherford-like scattering effect, induced by an attractive/repulsive potential, should deflect electron trajectories and hence ease or hinder electron injection in the QR arms. The injection of electrons has been shown to be critical in mesoscopic devices [6,22], and our results provide direct confirmation that even small changes in the electrostatic potential at a specific location in the device have

*sebastien.toussaint@uclouvain.be
†benoit.hackens@uclouvain.be

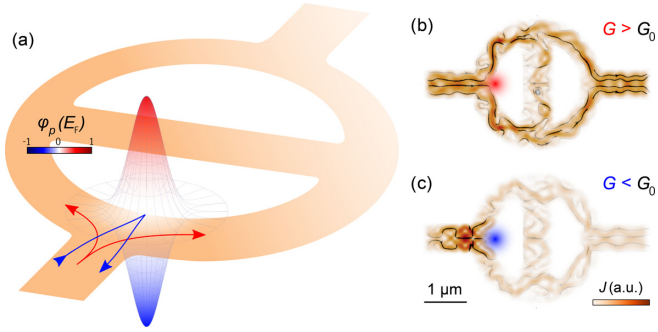

FIG. 1. (a) Illustration of the ringlike geometry (orange, not on scale), with the superimposed potentials used to tailor the potential landscape next to the edge of the ring antidot. (b) and (c) Tight-binding simulations of the current density modulus J associated with the first electronic mode and isocurrent density lines (black lines with arrows) for depletion (red potential) and accumulation (blue potential), respectively. G_0 is the total conductance without any perturbation potential.

strong impacts on ballistic charge transmission and hence on the device conductance. Experiments fully reproduce the simulated behavior by applying positive or negative potentials on a scanning metallic tip positioned over the hard wall. Counterintuitively, the highest conductance is observed for a depleting tip potential and vice versa.

II. RESULTS AND DISCUSSION

Quantum transport simulation results were obtained using the KWANT package [23] for the ringlike geometry depicted in Fig. 1, where device boundaries are defined by infinitely sharp hard walls. We focus here on the two T-shaped junctions located next to its leads, as this is where ballistic trajectories will be tuned. Note that the central branch connecting the two circular arms plays no role in this work.

The colored regions in Fig. 1(a) correspond to either raised (red) or lowered (blue) potential with respect to the otherwise flat background potential (disorder will be introduced later in the paper). This color convention will be followed throughout the paper: red indicating depleting perturbation (raised potential) and blue indicating accumulating perturbation (lowered potential). Figures 1(b) and 1(c), corresponding to the simulated current density distribution (associated with the first electronic mode) in the potential landscapes of Fig. 1(a), visually illustrate the impact of reversing the added potential experienced by electrons impinging on the T junction. In Fig. 1(b), the current injected through the left contact is favorably redirected towards the lateral branches of the device. In contrast, Fig. 1(c) reveals that current lines are focused on the hard wall, which enhances reflection back to the entrance lead.

At this point it seems that current redirection might yield a strong signature in the device conductance G, which may look counterintuitive at first sight: simulations indeed predict that a repulsive perturbation should increase G, while an attractive potential should degrade it. Furthermore, one can wonder how sensitive this peculiar focusing/defocusing behavior is with respect to the amplitude, spatial extension, and location of

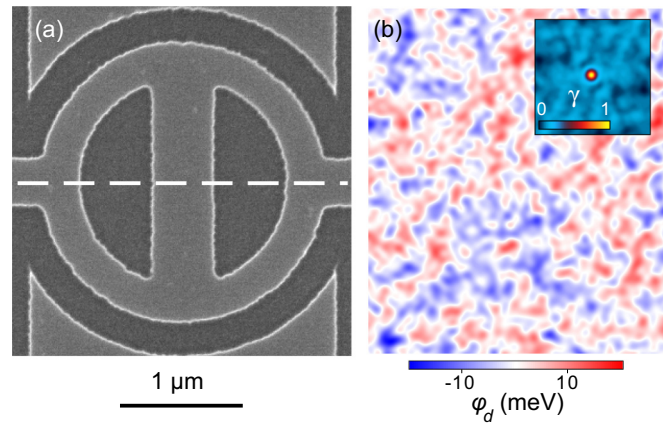

FIG. 2. (a) Scanning electron micrograph of the fabricated sample in an InGaAs/InAlAs heterostructure. (b) Computed real-space disorder potential φ_d at the level of the 2DEG that will be used in the forthcoming simulations. The disorder standard deviation S_d is 4.78 meV, calculated taking into account a distribution of Si ionized dopants located 20 nm above the 2DEG (i.e., the thickness of the InAlAs spacer). The inset in (b) shows a map of the autocorrelation as the correlation lag becomes a vector in the x-y plane.

the introduced potential perturbation presented in Fig. 1, as well as to the disorder in the background potential. The effect of all these parameters will be simulated in detail later in the paper where transmission through the device, converted to conductance, will be computed. In addition, it is tempting to test these predictions by measuring the conductance of a real-world device.

We thus carved out a ringlike structure from an InGaAs/InAlAs heterostructure hosting a 2DEG. The device geometry shown in Fig. 2(a) is lithographically very comparable to the one simulated above (the layer structure is similar to the one described in Ref. [24]). The 2DEG density and mobility can be tuned thanks to an applied electrostatic back-gate potential V_{BG}. The following data were measured at the maximal accessible charge carrier density ($\sim 10^{16}$ m^{-2}) and mobility (~ 10 m^2/Vs) corresponding to $V_{BG} = 4$ V. The Fermi energy is thus $E_F = 55$ meV, and the Fermi wavelength is $\lambda_F = 25$ nm. The four-contact conductance measurements were performed at a temperature $T = 40$ mK using a standard lock-in technique with a bias that remained comparable to $\frac{k_B T}{e}$. The physical characteristics of the host heterostructure allowed the modeling of the fixed disorder potential represented in Fig. 2(b) that will be used in the forthcoming simulations. The disorder potential φ_d models the influence of randomly positioned singly ionized silicon dopants located in a plane 20 nm away from the InGaAs 2DEG. Screening of the dopant potential by the 2DEG is taken into account via the Thomas-Fermi model (where we consider Lindhard's dielectric function). The amplitude of disorder is estimated in the plane where the wave function for the ground state along the confinement direction (z axis) takes its average value. This wave function is solved within the Fang-Howard variational approach (which was found to differ only marginally from a three-dimensional (3D) self-consistent Poisson-Schrödinger simulation).

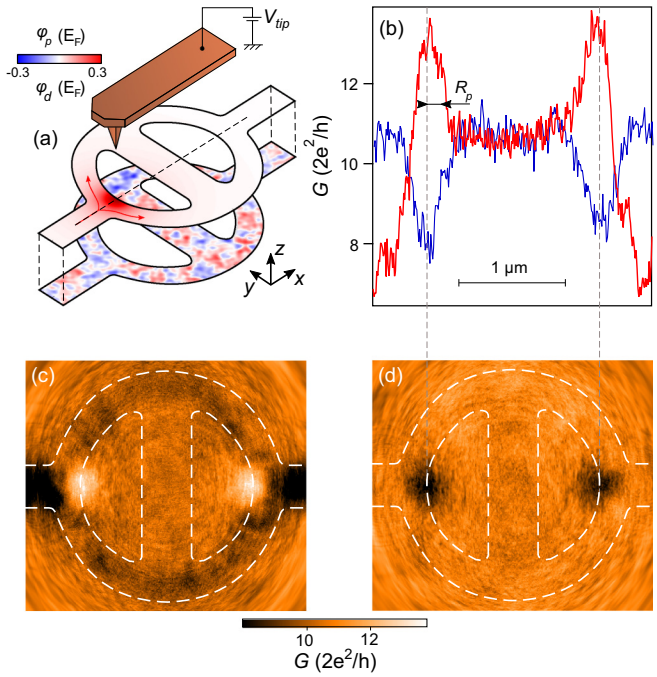

FIG. 3. (a) Illustration of the potential used for the simulations. It is composed of a disorder potential φ_d and a Lorentzian-shaped perturbation potential φ_p caused by a biased conductive AFM tip located above the 2DEG. (b) Simulated conductance profiles as φ_p is swept along the dashed line in (a). Simulation parameters are as follows (same conditions as in Fig. 1, except for disorder): the red profile corresponds to $\varphi_p^{\max} = 0.9E_F$ (depletion) and $R_p = 150$ nm; the blue profile corresponds to a reversed perturbation potential (accumulation; $\varphi_p^{\max} = -0.9E_F$). These profiles are extracted from the conductance mapping obtained when φ_p is swept in the (x, y) plane. They are presented in (c) ($\varphi_p > 0$) and (d) ($\varphi_p < 0$). The vertical dashed lines correspond to the locations of the hard walls along the scanned line in (a).

Experimentally, a convenient way to generate the kind of perturbation potential used in the simulations presented above is by approaching an electrically biased nanoscale tip V_{tip} at a distance d_{tip} above the patterned quantum ring [as illustrated in Fig. 3(a)]. The tip can then be scanned along the transport direction, i.e., along the dashed lines in Figs. 2(a) and 3(a). In order to achieve a large effect, we brought the tip to a distance $d_{\text{tip}} = 60$ nm above the sample surface and biased the tip with large positive and negative voltages up to $|V_{\text{tip}}| = 14$ V.

The presence of the biased conductive Atomic Force Microscope (AFM) tip is numerically modeled using a Lorentzian-shaped perturbation potential $\varphi_p(x, y)$ [illustrated in Fig. 1(a)] parametrized by the position of its center $(x_{\text{tip}}, y_{\text{tip}})$, height ${\varphi_p}^{\max}$, and width R_p, which is half the potential FWHM. The superposition of $\varphi_p(x, y)$ on the modeled disordered potential φ_d, together with the hard-wall boundaries that mark the edges of the nanodevice, defines the potential landscape used in the simulations.

In Fig. 3(b), the conductance is computed as φ_p moves along the axis joining the entrance and the exit contacts [dashed lines in Figs. 2(a) and 3(a)]. Remarkably, when the tip position stands near the location of the hard wall (vertical dashed lines), the conductance significantly deviates from that in the absence of perturbation ($\sim 11 \times \frac{2e^2}{h}$), e.g., when the tip stands at the center of the device. Beyond fluctuations originating from the presence of the random disorder, the effect is symmetric because positioning the tip near both T junctions gives the same result. More importantly, this behavior is somewhat counterintuitive: while a repulsive potential close to both T junctions actually helps electrons crossing the overall structure (enhanced conductance), an attractive perturbation reduces their ability to pass through the device.

Looking further in the simulation results, we observe that reversing the sign of φ_p essentially reverses the change in conductance. Surprisingly, the backscattering to the leads, due to current focusing on the hard-wall potential of the antidot [described in Figs. 1(a) and 1(c)], is similar in amplitude to the enhanced transmission due to defocusing [Figs. 1(a) and 1(b)]. On the other hand, we observe that the symmetric behavior observed when changing the sign of φ_p naturally breaks when the tip locates above the leads. In that case, while depleting the lead strongly reduces the conductance, accumulating electrons naturally has a much weaker effect. Finally, when moving the perturbation from the T junction area towards the center of the device, the effect on G naturally vanishes over a distance corresponding roughly to R_p [Fig. 3(b)].

Besides moving the tip along the device axis, one can also wonder how sensitive G variations are to the perturbation position in the (x, y) plane. This aspect is examined in the G maps plotted in Figs. 3(c) and 3(d) obtained for locally raised and lowered moving potentials, respectively. The main contrast is observed over the T junctions as well as over the device leads for a depleting potential. In both the x and y directions, this contrast fades away over distances comparable to R_p. When positioning the perturbation potential over the device arms and their vicinities, the G map is decorated with short, characteristic length-scale fluctuations which are similar to those reported in previous works [25–27]. This weaker amplitude contrast was attributed to the perturbation of resonant states in the local density of states (LDOS) by the moving potential [25,26], as well as to the electrostatic Aharonov-Bohm effect [27]. Note that here the mapping conditions are not suitable for imaging the LDOS because the moving potential is in the strong perturbation and not in the linear regime discussed in Ref. [25]. In this framework we are not using the scanning gate with microscopy purposes in mind.

It is now time to compare these predictions with experimental results obtained for the sample described above. Figure 4 summarizes the data in a way to ease the comparison with the simulations. We first scanned the biased tip along a line linking the device leads for two opposite-sign voltage biases. Figure 4(a) shows, like the simulations in Fig. 3(b), that a depleting (red) potential, near the border of the inner quantum dot, eases electron injection, while an accumulating potential (blue) located at the same place tends to reduce electron transmission through the device.

For a strongly depleting potential [$V_{\text{tip}} = -14$ V; red curve in Fig. 4(a)], corresponding roughly to $\varphi_p^{\max} \sim 0.4E_F$ (see Fig. S2 in the Supplemental Material [28]), G exhibits local maxima when the tip is located above the limit of the etched area in front of the entrance and exit leads [dashed lines in Fig. 4(a)]. As expected, the conductance is reduced further as the tip decreases the 2DEG density over the leads.

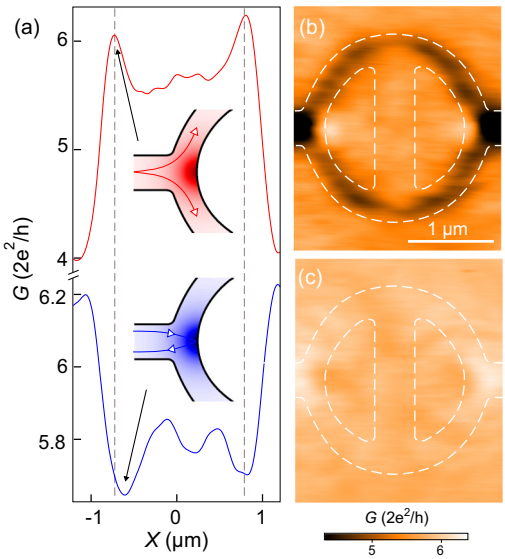

FIG. 4. (a) Experimental conductance profile as a voltage-biased tip is scanned along the dashed line presented in Fig. 2(a). The tip is scanned at a distance of 60 nm from the sample surface with $V_{\text{tip}} = -14$ V (red curve) or $+8$ V (blue curve). A qualitative scenario is also illustrated for the peculiar electron forward scattering (red) and backscattering (blue). (b) Conductance map as the biased tip ($V_{\text{tip}} = -14$ V, depletion) is scanned in a plane at the same constant distance from the sample surface. (c) Same map as the one presented in (b), but with $V_{\text{tip}} = +8$ V (accumulation).

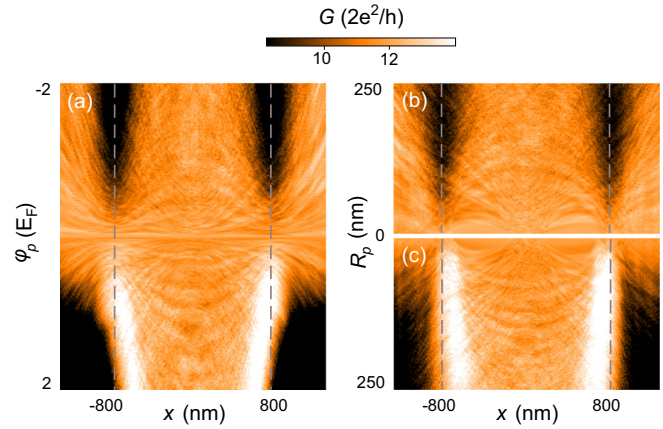

FIG. 5. Simulated conductance profiles as the potential perturbation is swept along the black dashed line in Fig. 3(a) for several values of (a) $\varphi_p^{\max}$ with $R_p = 150$ nm and disorder strength $S_d = 4.78$ meV, (b) R_p with $\varphi_p^{\max} = -0.9E_F$ and $S_d = 4.78$ meV, and (c) R_p with $\varphi_p^{\max} = 0.9E_F$ and $S_d = 4.78$ meV. The vertical dashed lines correspond to the locations of the hard walls along the scanned line.

But, counterintuitively, a strongly accumulating potential ($V_{\text{tip}} = 8$ V) brings G to a minimum. Moreover, the effect is essentially symmetric when the tip moves from one T branch to the other. The qualitative match with the curves presented in Fig. 3(b) (obtained for $\varphi_p^{\max} = \pm 0.9E_F$) is very good [29], and the experimental conductance maps presented in Figs. 4(b) and 4(c) (the same data as in Fig. 4(c) are presented in the Supplemental Material with an enhanced contrast [30]) compare well with the simulations presented in Figs. 3(c) and 3(d). We observe a remarkable coincidence of simulated and experimental positions and lateral extensions of the peaks and dips located around the hard walls in the T junctions. Note also that, in addition to the main dips and peaks discussed above, some fluctuations are visible in the experimental data in Fig. 4(a), in particular when moving the tip towards the center of the device. Such fluctuations are reproducible and associated with universal conductance fluctuations [31] (UCFs), stemming from tip-induced changes in the potential causing phase and momentum changes for charge carriers at the local scale, thereby affecting charge carrier interferences. The amplitude of similar fluctuations is larger in the simulation results shown in Fig. 3(b), as temperature in the simulations is 0 K, so thermal smearing and decoherence are not taken into account.

Resonant features along the ring circumference are also observed in all cases, but the smallest ones that are visible in simulated G maps in Figs. 3(c) and 3(d), in particular those with a concentric shape observed mostly outside the device area, are absent in the experimental data. This is most likely related to thermal averaging, which is not taken into account in the simulations.

At this stage, we can conclude that the experiments confirm, at least qualitatively, that a focusing/defocusing can be induced by a Lorentzian perturbation combined to a hard-wall potential in a ballistic device. While defocusing [Fig. 4(a), red] is clearly reminiscent of the Rutherford scattering, here in two dimensions, focusing on the hard wall induces a peculiar backscattering mechanism as the lensing is combined with the specular reflection illustrated in Fig. 4(a) (blue).

At first sight, the weaker absolute value of the voltage applied on the tip in accumulation [blue in Fig. 4(a)] could explain why the effect on the conductance is weaker than in depletion [red in Fig. 4(a)]. However, we need to dig deeper in the simulations to test the quantitative correspondence between experiments and predictions.

Figure 5 shows the evolution of the conductance when φ_p travels along the axis of the quantum ring and when either $\varphi_p^{\max}$ or R_p is varied, with the other parameters remaining constant (a similar map with a varying disorder amplitude S_d is shown in the Supplemental Material [32]). We obviously focus our attention on the two regions near the edge of the inner QR, i.e., $x \sim \pm 800$ nm [dashed lines in Figs. 5(a) and 5(b)]. We first observe no obvious threshold when $|\varphi_p^{\max}|$ increases [Fig. 5(a)]. G undergoes a smooth evolution at least up to $2E_F$. However, on the depletion side ($\varphi_p > 0$), the positions of the local G maxima are gradually shifting towards the center of the device as $\varphi_p^{\max}$ is made more positive. This reflects the fact that roughly identical potential perturbation conditions are found in the T junctions for both a weakly perturbing potential ($\varphi_p^{\max} < E_F$) centered close to the hard wall and a strongly perturbing potential ($\varphi_p^{\max} > E_F$) centered farther away from the hard wall. On the accumulation side ($\varphi_p < 0$), the position of the dips' centers remains essentially unaffected: charge accumulation in the T junctions does not modify their geometry.

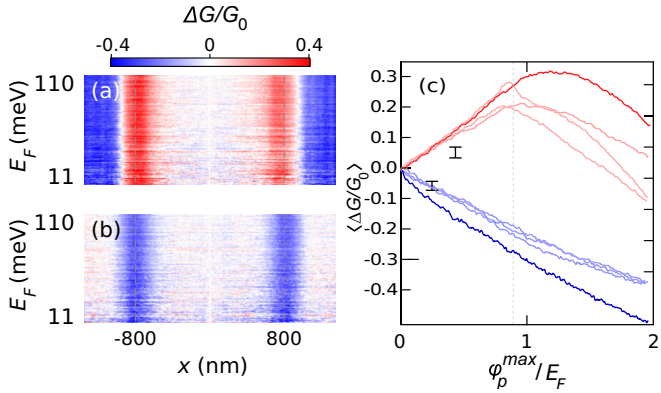

FIG. 6. (a) and (b) Relative variation of conductance $\Delta G/G_0$ with respect to that at $x = 0$ for $\frac{|\varphi_p^{\max}|}{E_F}$ fixed at 0.9 for all E_F in the presented range. (a) is a map realized for a depleting tip-induced potential, and (b) is for an accumulating tip. (c) Relative conductance variation, averaged over the range 11 meV $< E_F <$ 110 meV, at $x = -800$ nm (red and blue show depletion and accumulation, respectively). These curves are obtained for different disorder configurations (keeping the same disorder standard deviation). The dark red and blue curves correspond to the disorder configuration that was used to generate all the simulated data presented, above and the light red and blue curves correspond to different disorder configurations. The two experimental data points are indicated in (c) in the form of two vertical bars.

Varying R_p has an interesting effect on the conductance peaks and dips. Beyond a few tens of nanometers and up to 200 nm, where the arms themselves start to become narrowed, varying R_p has essentially no effect on the amplitude of conductance extrema for either negative [Fig. 5(b)] or positive [Fig. 5(c)] perturbation potentials. Indeed, the amplitude of conductance peaks and dips saturates for $R_p \geqslant \lambda_F = 25$ nm, i.e., in the classical regime (see the Supplemental Material [33]).

On the other hand, the evolution of the width of conductance extrema [Figs. 5(b) and 5(c)] is smoother and gives us the possibility to determine the value of R_p^{exp} that characterizes our experimental configuration. Based on the FWHM of the strongest (red) conductance peaks in Fig. 4(a), we obtain that $R_p^{exp} \sim 135$ nm. This value is well within the range investigated in the simulations and is indeed consistent with data discussed in the Supplemental Material.

Finally, our results show that increasing the disorder dampens the effect, but no qualitative change is observed even when multiplying the initial disorder [Fig. 2(b)] by a factor of 4 (see Fig. S1 in the Supplemental Material). This robustness is a clear signature that distinguishes the present effect from UCFs. Indeed, in constrast with the smooth and continuous evolution observed in Fig. S1 in the Supplemental Material, the random nature of UCFs should lead to large (on the scale of $2e^2/h$) and uncorrelated variations of conductance when an external parameter, such as S_d, is varied.

To go beyond the good qualitative correspondence between Figs. 3 and 4, we now need to question the experimental data more quantitatively. This is the purpose of Fig. 6, which addresses the effect of the density, or Fermi energy, and finally provides a quantitative comparison between experiments and simulations.

The simulated variation of the conductance with E_F, while keeping constant the absolute value of the ratio $\frac{\varphi_p^{\max}}{E_F} = 0.9$, is presented in Fig. 6(a) for depleting tip-induced potential and in Fig. 6(b) for accumulating tip-induced potential. Since G increases with E_F, it makes sense to examine the relative change in conductance $\Delta G/G_0 = (G - G_0)/G_0$, where G_0 is the conductance of the device when the tip is above the device center ($x = 0$). It is immediately apparent that the simulated $\Delta G/G_0$ is insensitive to E_F provided that the ratio $\varphi_p^{\max}/E_F$ is kept constant at 0.9. In other words, the efficiencies of both focusing and defocusing are not sensitive to E_F alone but, as Fig. 6(c) clearly reveals, to the ratio $\frac{\varphi_p^{\max}}{E_F}$. More precisely, Fig. 6(c) shows a linear dependence of $\Delta G/G_0$ as a function of $\frac{\varphi_p^{\max}}{E_F}$ up to $\frac{\varphi_p^{\max}}{E_F} \simeq 1$ in the depletion regime. It is noteworthy that the linear behavior is only weakly sensitive to disorder in this regime. For $\frac{\varphi_p^{\max}}{E_F} \geqslant 1$, defocusing by a depleting tip becomes less efficient as the arms' width starts to shrink, and the overall behavior is much more sensitive to the precise disorder configuration. No such deviation from linearity is observed in the case of accumulation [blue lines in Fig. 6(c)]. The counterintuitive entry/exit symmetry persists in the whole range investigated, and the linearity with respect to $\frac{\varphi_p^{\max}}{E_F}$ is preserved.

How can we understand this linear dependence, at least in the depletion regime? The defocusing of ballistic electrons facing a Lorentzian-shaped repulsive potential is clearly reminiscent of Rutherford scattering. The original Rutherford formalism provides an expression for the differential cross section in three dimensions for a scattering potential $\frac{C}{r}$, where C is the amplitude and r is the distance from the scattering center, as a function of the energy of incident particles E and of the scattering angle θ. Since the arms of the quantum ring capture electrons in a finite angle range from the leads, one can consider the differential cross section at a given angle to be related to the conductance of our ballistic device. Coincidentally, in the 3D case, the Rutherford formula is independent of whether you treat particles classically or quantumly [4]. In two dimensions, this elegant result is no longer valid in general. In the 2D quantum regime, one has to find an analytical expression of the differential cross section $\frac{d\lambda}{d\theta}$ by solving the 2D version of the Lippmann-Schwinger equation [34] with a Lorentzian-shaped potential distribution, which is far beyond the scope of the present work. In the 2D classical regime, however, an equivalent formula was derived [4,35]. For the same $\frac{C}{r}$ potential,

$$\frac{d\lambda}{d\theta} = \frac{|C|}{4E\sin^2(\theta/2)}. \quad (1)$$

One readily finds from Eq. (1) that, for a given angle θ, the scattering amplitude is fully determined by the ratio between the amplitude C of the perturbative potential and the energy of the particles. In the case of our device, this ratio would correspond to $\frac{\varphi_p^{\max}}{E_F}$. The linear response of the simulated $\Delta G/G_0$ with respect to changes in $\frac{\varphi_p^{\max}}{E_F}$ revealed in Fig. 6(c) is thus reminiscent of the 2D Rutherford scattering in the classical regime. Note that Eq. (1) is also valid in the accumulation regime, but in our QR geometry, specular reflection on the hard wall must also be taken into account. Beyond Eq. (1),

which is probably not strictly applicable to our Lorentzian-shaped potential, the Rutherford analogy helps us visualize the observed ballistic defocusing.

We finally turn to what is probably the most important information presented in Fig. 6(c): the quantitative comparison between experiments and simulations. To reach that point, we first need to evaluate the amplitude of the perturbation potential induced by the tip. A direct view of the shape of the tip-induced potential experienced by electrons inside the device is obtained by mapping the conductance of a narrow channel in a similar device (whose width is comparable to the leads of the device) close to pinch-off as a function of the electron density, with the tip scanning along a line perpendicular to the channel axis (see Supplemental Material, Fig. S2; this second device is located on the same sample). Following this procedure, we determined that $\varphi_p^{\max} = 3.9$ meV for $V_{\text{tip}} = -4$ V and $d_{\text{tip}} = 80$ nm and scaled this value while taking into account the parameters used in Fig. 3(a). Knowing the values of $\varphi_p^{\max}$ for both the depletion and accumulation potential data in Fig. 4(a), we were able to plot the experimental $\Delta G/G_0$ vs $\frac{\varphi_p^{\max}}{E_F}$ in Fig. 6(c) for two different values of $\varphi_p^{\max}/E_F$. The good agreement between experiments and simulations reveals the global consistency of our study and that it is indeed possible to strongly enhance or reduce the injection of ballistic electrons in a ballistic device by tuning the shape of the potential faced by electrons. It also means that the simple tight-binding model used here captures the essential physics of the phenomena. In the experiment, a conductance change of up to $\sim 10\%$ relative to the unperturbed device conductance is observed, which is relatively important, compared to, e.g., coherent effects at this temperature (40 mK). The phenomenon seems also particularly robust with respect to disorder. This may seem surprising at first sight if its origin is a "ballistic redirecting effect" induced by the tip potential. However, high-contrast magnetic focusing effects were observed in semiconductor heterostructures with comparable or lower mobilities [36]. This common robustness in both cases further reinforces the idea that ballistic focusing is at the heart of the observed phenomenon.

III. CONCLUSION

In conclusion, we have evidenced surprising ballistic electron focusing and defocusing behaviors governed by a local electrostatic potential. The phenomenology is similar to the 2D Rutherford scattering assuming classical electron dynamics. The applicability of this relatively simple classical formalism in the case of a 2DEG-based device was not expected. Indeed, the scattering amplitude for the interaction between charged particles and a sharp electrostatic potential should, in principle, be governed by complex interactions related to the presence of the many-particle background of the Fermi sea [8]. Another unexpected result of this work resides in the unexpected symmetry revealed between the amplitude of the Rutherford defocusing effect (when a depleting potential is applied) and reflective focusing, as experienced by electrons scattered by an accumulating potential in front of a hard wall. All these puzzling fundamental questions will require additional scrutiny and will probably foster further experimental and theoretical work.

In a broader context, our observations help in the understanding of charge carrier injection in ballistic devices, as they show that fine tuning of the potential in the vicinity of the entrance and exit leads can have huge effects on transmission through the whole device. In turn, this work provides useful tools in the perspective of building "electron optics" devices, where a local modulation of the electrostatic potential inside a device redirects the electron flow in a way similar to how an optical lens curves light rays [37]. In this framework, scanning gate microscopy can play an important role, as pointed out in various theoretical proposals where scattering was investigated by tuning the electrostatic potential at the local scale using a charged metallic tip [8,38,39]. Although the description of scattering in two spatial dimensions was considered a curiosity up to the early 1980s [35], nowadays high-mobility two-dimensional charge systems give this fundamental question complete relevance, and the possibility of testing this description, even with relativistic Dirac particles [40–43], also opens new directions of research.

ACKNOWLEDGMENTS

The authors acknowledge fruitful discussions with Prof. T. Ihn about simulation of disorder. Computational resources were provided by the supercomputing facilities of the Université catholique de Louvain (CISM/UCL) and the Consortium des Equipements de Calcul Intensif en Fédération Wallonie Bruxelles (CECI) funded by the FNRS - Belgian National Fund for Scientific Research. S.T. gives special thanks to D. François for his valuable help concerning parallel computing. This work was funded by the Fonds de la Recherche Scientifique FRS-FNRS (Grants No. J.0067.13, No. T.0172.13, No. 326 U.N025.14, No. J.0009.16, and No. 2450312F) and by the Communauté Française de Belgique (ARC Grant No. 11/16-037, Stresstronics Project and ARC Grant No. 16/21-077, NATURIST Project). S.T. is funded by a Fonds pour la Formation à la Recherche dans l'Industrie et dans l'Agriculture FRIA fellowship. B.H. acknowledges support as a FRS-FNRS research associate.

[1] E. Rutherford, London, Edinburgh, Dublin Philos. Mag. J. Sci. **21**, 669 (1911).

[2] H. Geiger and E. Marsden, Proc. R. Soc. London, Ser. A **82**, 495 (1909).

[3] G. Aad, E. Abat, J. Abdallah, A. Abdelalim, A. Abdesselam, O. Abdinov, B. Abi, M. Abolins, H. Abramowicz, E. Acerbi *et al.*, J. Instrum. **3**, P07007 (2008).

[4] H. Friedrich, *Scattering Theory*, Lecture Notes in Physics Vol. 872 (Springer, Berlin, 2013).

[5] S. Datta, *Electronic Transport in Mesoscopic Systems* (Cambridge University Press, Cambridge, 1997).

[6] A. A. Sousa, A. Chaves, G. A. Farias, and F. M. Peeters, Phys. Rev. B **88**, 245417 (2013).

[7] D. S. Saraga, B. L. Altshuler, D. Loss, and R. M. Westervelt, Phys. Rev. Lett. **92**, 246803 (2004).

[8] D. S. Saraga, B. L. Altshuler, D. Loss, and R. M. Westervelt, Phys. Rev. B **71**, 045338 (2005).

[9] B. J. van Wee, H. van Houten, C. W. J. Beenakker, J. G. Williamson, L. P. Kouwenhoven, D. van der Marel, and C. T. Foxon, Phys. Rev. Lett. **60**, 848 (1988).

[10] D. A. Wharam, T. J. Thornton, R. Newbury, M. Pepper, H. Ahmed, J. E. F. Frost, D. G. Hasko, D. C. Peacock, D. A. Ritchie, and G. A. C. Jones, J. Phys. C **21**, L209 (1988).

[11] K. J. Thomas, J. T. Nicholls, M. Y. Simmons, M. Pepper, D. R. Mace, and D. A. Ritchie, Phys. Rev. Lett. **77**, 135 (1996).

[12] S. M. Cronenwett, H. J. Lynch, D. Goldhaber-Gordon, L. P. Kouwenhoven, C. M. Marcus, K. Hirose, N. S. Wingreen, and V. Umansky, Phys. Rev. Lett. **88**, 226805 (2002).

[13] M. Topinka, B. LeRoy, R. Westervelt, S. Shaw, R. Fleischmann, E. Heller, K. Maranowski, and A. Gossard, Nature (London) **410**, 183 (2001).

[14] B. Brun, F. Martins, S. Faniel, B. Hackens, G. Bachelier, A. Cavanna, C. Ulysse, A. Ouerghi, U. Gennser, D. Mailly, S. Huant, B. Vincent, S. Marc, and H. Sellier, Nat. Commun. **5**, 4290 (2014).

[15] B. Brun, F. Martins, S. Faniel, B. Hackens, A. Cavanna, C. Ulysse, A. Ouerghi, U. Gennser, D. Mailly, P. Simon, S. Huant, V. Bayot, M. Sanquer, and H. Sellier, Phys. Rev. Lett. **116**, 136801 (2016).

[16] A. M. Song, A. Lorke, A. Kriele, J. P. Kotthaus, W. Wegscheider, and M. Bichler, Phys. Rev. Lett. **80**, 3831 (1998).

[17] A. Song, P. Omling, L. Samuelson, W. Seifert, I. Shorubalko, and H. Zirath, Appl. Phys. Lett. **79**, 1357 (2001).

[18] L. Bednarz, B. Hackens, G. Farhi, V. Bayot, and I. Huynen, Solid State Commun. **134**, 217 (2005).

[19] K. E. Aidala, R. E. Parrott, T. Kramer, E. Heller, R. Westervelt, M. P. Hanson, and A. C. Gossard, Nat. Phys. **3**, 464 (2007).

[20] S. Bhandari, G.-H. Lee, A. Klales, K. Watanabe, T. Taniguchi, E. Heller, P. Kim, and R. M. Westervelt, Nano Lett. **16**, 1690 (2016).

[21] C. Pöltl, A. Kozikov, K. Ensslin, T. Ihn, R. A. Jalabert, C. Reichl, W. Wegscheider, and D. Weinmann, Phys. Rev. B **94**, 195304 (2016).

[22] A. Chaves, G. A. Farias, F. M. Peeters, and B. Szafran, Phys. Rev. B **80**, 125331 (2009).

[23] C. W. Groth, M. Wimmer, A. R. Akhmerov, and X. Waintal, New J. Phys. **16**, 063065 (2014).

[24] S. Toussaint, F. Martins, S. Faniel, M. G. Pala, L. Desplanque, X. Wallart, H. Sellier, S. Huant, V. Bayot, and B. Hackens, Sci. Rep. **8**, 3017 (2018).

[25] F. Martins, B. Hackens, M. G. Pala, T. Ouisse, H. Sellier, X. Wallart, S. Bollaert, A. Cappy, J. Chevrier, V. Bayot, and S. Huant, Phys. Rev. Lett. **99**, 136807 (2007).

[26] R. Crook, C. G. Smith, A. C. Graham, I. Farrer, H. E. Beere, and D. A. Ritchie, Phys. Rev. Lett. **91**, 246803 (2003).

[27] B. Hackens, F. Martins, T. Ouisse, H. Sellier, S. Bollaert, X. Wallart, A. Cappy, J. Chevrier, V. Bayot, and S. Huant, Nat. Phys. **2**, 826 (2006).

[28] See Fig. S2 in the Supplemental Material at http://link.aps.org/supplemental/10.1103/PhysRevB.98.075310 for a characterization of the tip-induced Lorentzian shape.

[29] A significant increase in conductance is observed in the experimental data when the accumulating tip stands above the entrance leads, which contrasts with the behavior observed in the simulated conductance [Fig. 3(b)], where no increase is found in the lead region. This can be explained by the different geometries in both cases: the simulated device has semi-infinite leads, without edge roughness, while the actual device has 400-nm-long leads, with some edge roughness due to chemical etching (on the scale of 10–20 nm). An accumulating tip can therefore enhance charge carrier injection in the actual device and can bring electrons away from the rough edges and therefore cause the device conductance to rise.

[30] See Fig. S4 in the Supplemental Material at http://link.aps.org/supplemental/10.1103/PhysRevB.98.075310 for the same data as those presented in Fig. 4(c) with a different color scale.

[31] P. A. Lee and A. D. Stone, Phys. Rev. Lett. **55**, 1622 (1985).

[32] See Fig. S1 in the Supplemental Material at http://link.aps.org/supplemental/10.1103/PhysRevB.98.075310 for an illustration of the disorder dependence of the phenomenon.

[33] See Fig. S3 in the Supplemental Material at http://link.aps.org/supplemental/10.1103/PhysRevB.98.075310 for the dependence of the conductance maximum with respect to half the tip-induced full width at half maximum.

[34] B. A. Lippmann and J. Schwinger, Phys. Rev. **79**, 469 (1950).

[35] G. Barton, Am. J. Phys. **51**, 420 (1983).

[36] B. Hackens, F. Delfosse, S. Faniel, C. Gustin, H. Boutry, X. Wallart, S. Bollaert, A. Cappy, and V. Bayot, Phys. Rev. B **66**, 241305 (2002).

[37] P. Bøggild, J. M. Caridad, C. Stampfer, G. Calogero, N. R. Papior, and M. Brandbyge, Nat. Commun. **8**, 15783 (2017).

[38] M. Braun, L. Chirolli, and G. Burkard, Phys. Rev. B **77**, 115433 (2008).

[39] J. Cserti, A. Pályi, and C. Péterfalvi, Phys. Rev. Lett. **99**, 246801 (2007).

[40] J.-S. Wu and M. M. Fogler, Phys. Rev. B **90**, 235402 (2014).

[41] S. Russo, J. B. Oostinga, D. Wehenkel, H. B. Heersche, S. S. Sobhani, L. M. K. Vandersypen, and A. F. Morpurgo, Phys. Rev. B **77**, 085413 (2008).

[42] D. Cabosart, S. Faniel, F. Martins, B. Brun, A. Felten, V. Bayot, and B. Hackens, Phys. Rev. B **90**, 205433 (2014).

[43] D. Cabosart, A. Felten, N. Reckinger, A. Iordanescu, S. Toussaint, S. Faniel, and B. Hackens, Nano Lett. **17**, 1344 (2017).